

First Observation of Antiproton Annihilation At Rest on Argon in the LArIAT Experiment

V. Basque,¹ R. Acciarri,¹ J. Asaadi,² M. Backfish,^{1,*} W. Badgett,¹ F. Cavanna,¹ W. Flanagan,³ W. Foreman,^{4,†} R. Gomes,⁵ E. Gramellini,⁶ M. A. Hernandez-Morquecho,⁴ J. Ho,^{7,‡} E. Kearns,⁸ E. Kemp,⁹ M. King,⁷ T. Kobilarcik,¹ P. Kryczyński,¹⁰ B. R. Littlejohn,⁴ A. Marchionni,¹ C. A. Moura,¹¹ J. L. Raaf,¹ D. Schmitz,⁷ M. Soderberg,¹² J. M. St. John,¹ and A. M. Szelc¹³
(LArIAT Collaboration)[§]

¹*Fermi National Accelerator Laboratory, Batavia, IL 60510, USA*

²*University of Texas at Arlington, Arlington, TX 76019, USA*

³*University of Dallas, Irving, Texas 75062, USA*

⁴*Illinois Institute of Technology, Chicago, IL 60616, USA*

⁵*Universidade Federal de Goiás, Goiás, CEP 74690-900, Brasil*

⁶*University of Manchester, Manchester M13 9PL, UK*

⁷*University of Chicago, Chicago, IL 60637, USA*

⁸*Boston University, Boston, MA 02215, USA*

⁹*Universidade Estadual de Campinas, Campinas, SP 13083-859, Brasil*

¹⁰*Institute of Nuclear Physics PAN, 31-342 Kraków, Poland*

¹¹*Universidade Federal do ABC, Santo André, SP 09210-580, Brasil*

¹²*Syracuse University, Syracuse, NY 13244, USA*

¹³*University of Edinburgh, Edinburgh, EH8 9YL, UK*

(Dated: September 23, 2024)

We report the first observation and measurement of antiproton annihilation at rest on argon using the LArIAT experiment. Antiprotons from a charged particle test beam that come to rest inside LArIAT’s liquid argon time projection chamber (LArTPC) are identified through beamline instrumentation and LArTPC track reconstruction algorithms. The multiplicity of charged particle tracks originating from the annihilation vertex is manually assessed through hand-scanning, resulting in a distribution with a mean of 3.2 ± 0.4 tracks and a standard deviation of 1.3 tracks. This is consistent with an automated track reconstruction, which produces a mean of 2.8 ± 0.4 tracks and a standard deviation of 1.2 tracks. Good agreement is found between data and Monte Carlo simulations for both methods. Additionally, we report the shower multiplicity and particle identification of outgoing tracks, both of which align closely with theoretical predictions. These findings will contribute to modeling of intranuclear annihilation interactions on argon, including scenarios such as neutron-antineutron oscillations.

I. INTRODUCTION

Due to their distinct “star-shaped” final-state topology, antiproton (\bar{p}) annihilations at rest have produced some of the most striking images in particle physics. First observed in 1955 at the Bevatron using photographic emulsion [1–3], \bar{p} annihilation on nucleons (N) have now been observed by a number of experiments, and on various target nuclei [4–16].

The $\bar{p}N$ annihilation takes place preferentially at the surface of a nucleus [17] and results in a set of particles, primarily pions (π), emanating isotropically from the annihilation vertex. The exact number and mixture of produced particle types varies depending on the target nucleus. Since a fraction of the pions from the annihilation have to travel through the nucleus before

becoming visible in the detector, they can undergo a number of final-state interactions (FSI) processes: absorption ($\pi^+ + n \rightarrow p$ or $\pi^- + p \rightarrow n$), neutral pion production ($\pi^\pm + n \rightarrow \pi^\pm + n + \pi^0$), quasi-elastic scattering ($\pi^\pm + N \rightarrow \pi^\pm + N$), or single-charge exchange ($\pi^+ + n \rightarrow p + \pi^0$ or $\pi^- + p \rightarrow n + \pi^0$). These processes modify the kinematics of the pions or even prevent pions from exiting the nucleus entirely.

Because of these FSI, final-states of $\bar{p}N$ annihilation can be used as a proxy for that of theorized neutron-antineutron ($n-\bar{n}$) oscillations [18] where the newly-converted \bar{n} immediately annihilates with a neighboring nucleon. Observing this baryon number violating process would satisfy one of the Sakharov conditions [19] and would have profound implications for theories on baryogenesis, the origin of matter-antimatter asymmetry, and large extra dimensions [20–23]. Assuming isospin symmetry, and the similarity of protons and neutrons in terms of quark content, it can be assumed that $\bar{p}N$ annihilation interactions result in outgoing products that are largely similar in particle makeup and kinematic distribution to those that would emerge from a $\bar{n}N$ annihilation [24]. Due to the difficulty in performing antineutron scatter-

* Current: University of California, Davis, CA 95616, USA

† Current: Los Alamos National Laboratory, Los Alamos, NM 87545, USA

‡ Current: Harvard University, Cambridge, MA 02138, USA

§ lariat_authors@fnal.gov

ing measurements and their resulting scarcity [25], $\bar{p}N$ annihilation are critical inputs for $n-\bar{n}$ oscillation models. More complete models, especially of FSI, are necessary to test automated reconstruction on these isotropic events to improve the sensitivity of future searches for $n-\bar{n}$ in large liquid argon time projection chambers (LArTPCs) like DUNE.

This paper presents the first-ever measurement of antiproton annihilation at rest on argon, performed with the liquid argon in a testbeam (LArIAT) experiment [26]. Antiproton are identified amongst the particles in the beamline, and a subset of these are identified as annihilating at rest inside a LArTPC. Their outgoing particles are compared to a dedicated Monte Carlo (MC) simulation of true antiprotons annihilating at rest in the LArTPC. The results presented here represent a first validation of the modeling of nucleon annihilation on argon and may be useful in constraining systematic uncertainties of FSI for pions produced by nucleon annihilation on argon.

II. THE LARIAT EXPERIMENT

The LArIAT experiment ran at Fermilab’s Test Beam Facility [27] situated in the Meson Center beam line. LArIAT’s primary purpose has measuring charged particle interaction cross sections and developing and calibration techniques. The LArIAT TPC operated in conjunction with a series of beamline monitoring subsystems to enable the triggering of detector readouts for individual particles that traverse the entire beamline and interact within the chamber.

Fermilab’s accelerator complex produces a 120 GeV/c primary proton beam which is focused onto a copper target to produce a secondary beam composed of primarily positively charged pions. The secondary beam momentum can be tuned between the range of 8 GeV/c to 80 GeV/c and was operated at 64 GeV/c for the datasets used in this analysis.

Before reaching LArIAT, the secondary beam entered the experimental hall enclosure where it struck a copper target inside a steel collimator to produce a tertiary beam of charged particles. The tertiary beam traveled through a series of beamline instrumentation elements as shown in Fig. 1: two (upstream, downstream) beam collimators (USCOLL, DSCOLL), two (upstream, downstream) time-of-flight (TOF) scintillating paddles (USTOF, DSTOF), four multi-wire proportional chambers (MWPCs), two bending dipole magnets (B1, B2), and a HALO scintillating paddle used to identify and veto particles entering the LArTPC that did not follow the path of the tertiary beamline. The trajectory of a charged particle traveling in the beamline was reconstructed by interpolating the straight segments obtained by at least 3 hits in the upstream MWPC (WC1 and WC2 in Fig. 1) in tandem with the downstream ones (WC3 and WC4 in Fig. 1). This reconstructs the particle’s trajectory before and after the bending magnets

which bends it in the xz -plane. The polarity of the magnets can be configured to select positively or negatively charged particles from the beam. The bending angle of the particle, together with the known magnetic field, are used to determine the particle’s momentum. The reconstructed beamline momentum for all triggered beamline particles in the dataset used for this analysis is shown in Fig. 2 using the -100 A magnet current. In addition, scintillator paddles are used to determine the particle’s TOF, which is used in tandem with the momentum to determine the particle mass as explained in Sec. III. Detailed discussion on the TOF and MWPC systems can be found in [26, 28].

Tertiary beamline particles were then directed into the LArTPC, a 170-liter active LAr volume approximately 90 cm in length (\hat{z} , along the beam direction), 47 cm in width (\hat{x}), and 40 cm in height (\hat{y}). The LArTPC and cryostat are shown in Fig. 3. The reference coordinate system used in LArIAT originates from the midpoint of the anode plane of the LArTPC. The z -direction aligns with the beam line, y -direction points upward, and x -direction extends from the anode to the cathode. The LArTPC readout comprised two readout-instrumented wire planes composed of 240 wires each (induction and collection), as well as a non-instrumented 225-wire shield plane. For the data-taking campaign used in this study, wires were spaced 4 mm apart with a 4 mm separation gap between each of the planes. The induction and collection wire planes were oriented at $\pm 60^\circ$ from the beamline direction. Ionization charge drifted along the \hat{x} direction from the cathode to the wire planes (anode) along a nominal field of 484 V/cm, which resulted in a maximum electron drift period of approximately 320 μ s. The LArIAT data acquisition system (DAQ) recorded the ionization produced by beamline particles traversing the LArTPC via induced or collected charge on the wire planes and these signals were digitized with a sampling period of 128 ns.

The analysis presented here uses beam-triggered data taken during 2016, referred to as Run II, when the tertiary beamline’s dipole magnets were operating with negative polarity in order to steer only negatively charged particles toward the LArTPC.

III. BEAMLINE RECONSTRUCTION AND ANTIPROTON SELECTION

All beamline triggered events are reconstructed to obtain their individual TOF and momentum as they traverse the beamline monitoring systems. It is possible to distinguish different particle types by utilizing the reconstructed TOF and momentum. This is shown in Fig. 4 with the overlapping expectations for particles present in the beam relevant for this analysis: the black solid curve is the expected deuteron region, in red the proton region, and in orange the kaon region. The dense region around 23 ns is where all lower minimally ionizing particles are

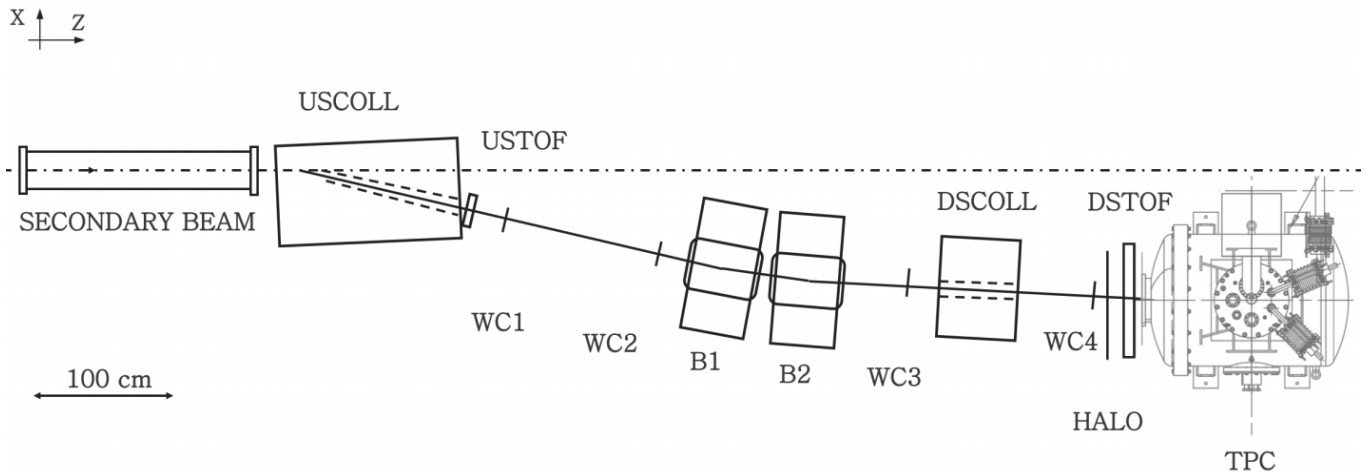


FIG. 1. Top-down view of LArIAT's tertiary beamline which shows the location and orientation of the beamline monitors and the technical drawing of the LArTPC. The monitors are labeled as follows: two (upstream and downstream) beam collimators (USCOLL and DSCOLL), two (upstream and downstream) time-of-flight scintillating paddles (USTOF and DSTOF), four multi-wire proportional chambers (WC1-WC4), two bending dipole magnets (B1 and B2), and a HALO scintillating paddle which was sensitive to particles which did not follow the path of the tertiary beamline. Figure is from [26].

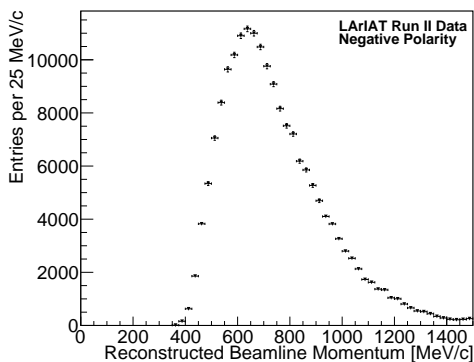


FIG. 2. Reconstructed beamline momentum spectrum for LArIAT's Run II at -100 A magnet current.

expected to be such as pions, muons, and electrons in green, blue, and purple, respectively. Faint horizontal bands present at TOF intervals of 20 ns are caused by multiple high-energy muons produced in the secondary beam far upstream of our tertiary beamline, with a time separation defined by the primary proton beam structure, which subsequently stream forward and separately strike the upstream and downstream TOF scintillator paddles creating a false TOF measurement for particular beam-triggered events.

The invariant beamline mass, m_b , for each triggered particle is calculated using its beamline-measured momentum, p_b , together with the measured TOF, t_{TOF} :

$$m_b = \frac{p_b}{c} \sqrt{\left(\frac{t_{\text{TOF}} \cdot c}{l}\right)^2 - 1}, \quad (1)$$

where c is the speed of light and l is the length traveled by



FIG. 3. Photograph showing the LArIAT TPC inserted into the inner cryostat.

the particle between the two TOF paddles, 6.65 m. The results for Run II negative polarity data for the calculation of the beamline masses are shown in Fig. 5. Particle types are classified according to three distinct regions as shown in the figure:

1. **electron, muon, pion:** 0 MeV/ c^2 to 375 MeV/ c^2 ,
2. **kaon:** 375 MeV/ c^2 to 650 MeV/ c^2 ,
3. **proton:** 800 MeV/ c^2 to 1100 MeV/ c^2 .

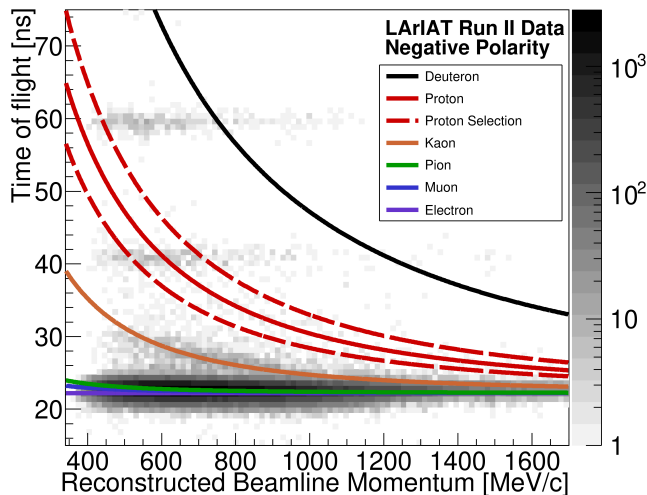


FIG. 4. Reconstructed beamline information for Run II negative-polarity data overlaid with the expectation curves of electrons, muon, pion, kaon, proton, and deuteron. In dashed is the mass selection cut of 800 MeV/c² to 1100 MeV/c² chosen in this analysis. The horizontal bands are due to the beam time structure producing false TOF measurements due to high-energy muons, produced by the secondary beam, which stream through the beamline instruments.

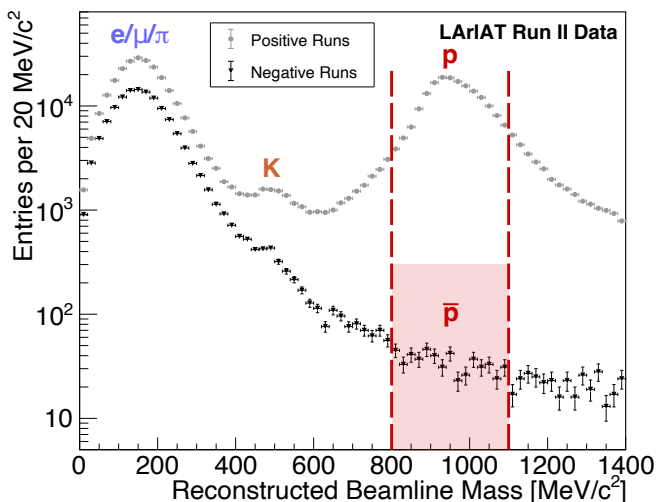


FIG. 5. Distribution of the reconstructed beamline mass for positive and negative polarity data runs. The distributions are divided into three major regions in order to distinguish muon/pion-like, kaon-like, and proton-like particle masses. The shaded red region shows where the selected antiprotons are located using the positive polarity proton selection cuts.

The beamline selection cuts chosen for this analysis are tuned using the Run II positive polarity data where there exists a large sample of protons ($\sim 100,000$). A selection using the reconstructed mass between 800 MeV/c² and 1100 MeV/c², inclusively, is chosen to include all of the proton-like mass peak while minimizing contamination

from kaons at lower mass and deuterons at higher mass. The selection is then applied to the data in Run II with -100 A magnet current used in this analysis to select the antiprotons. The impact of this selection cut is evident in the TOF and reconstructed beamline momentum distributions, as shown in Fig. 4, with the dashed curves the selected region for the antiprotons. Out of the $\approx 189,000$ events processed in the Run II negative polarity dataset, 520 are selected as having a mass consistent with an antiproton. The region selected is shown by the red shaded region in Fig. 5.

Kaons could mimic incoming beamline candidates in the case of short beam particle track length due to their similar energy deposition profile. To assess potential kaon contamination in the sample, a combined fit was applied to the negative polarity data from Fig. 5, with a Gaussian function centered at the kaon mass of ~ 494 MeV/c² on top of a Landau function to model the non-kaon beam related backgrounds in the calculated mass distribution. These backgrounds fitted by the Landau are actually accidental TOFs from 20 ns-space halo muons striking the TOF paddles. Since the events in these horizontal bands are due to random firings of the trigger from muons produced upstream of the tertiary beamline, they feature a high number of tracks in the TPC with no clear stopping beam-matched track. These are unlikely to contaminate the sample and are removed during the LArTPC selection stage. Based on an extrapolation of the fit into the proton-mass selection window, expected contamination of kaons is highly negligible, with $< 10^{-3}$ events expected for the full Run II sample.

IV. LArTPC RECONSTRUCTION AND AT-REST ANNIHILATION SELECTION

Following the antiproton beamline reconstruction and selection of Sec. III, the second reconstruction and selection phase happens in the LArTPC. In this phase, LArTPC data analysis employs a hybrid manual/automated reconstruction process, culminating in the determination of final candidates on an event-by-event basis using hand-scanning and hand-clustering methods as well as utilizing a ranged-based particle identification (PID) algorithm on both the incoming antiprotons and the outgoing particles from the annihilation vertex.

A. LArTPC Reconstruction & Simulation

LArTPC reconstruction is performed using the LArSoft (version 06.61.00) event processing framework [26, 28, 29] with outputs reconstructed particle objects and their associated kinematics. Particles passing through the LArTPC are reconstructed from ionization signals detected on the wires. These signals are waveforms of ADCs vs. time ticks; so-called “hits” within the wave-

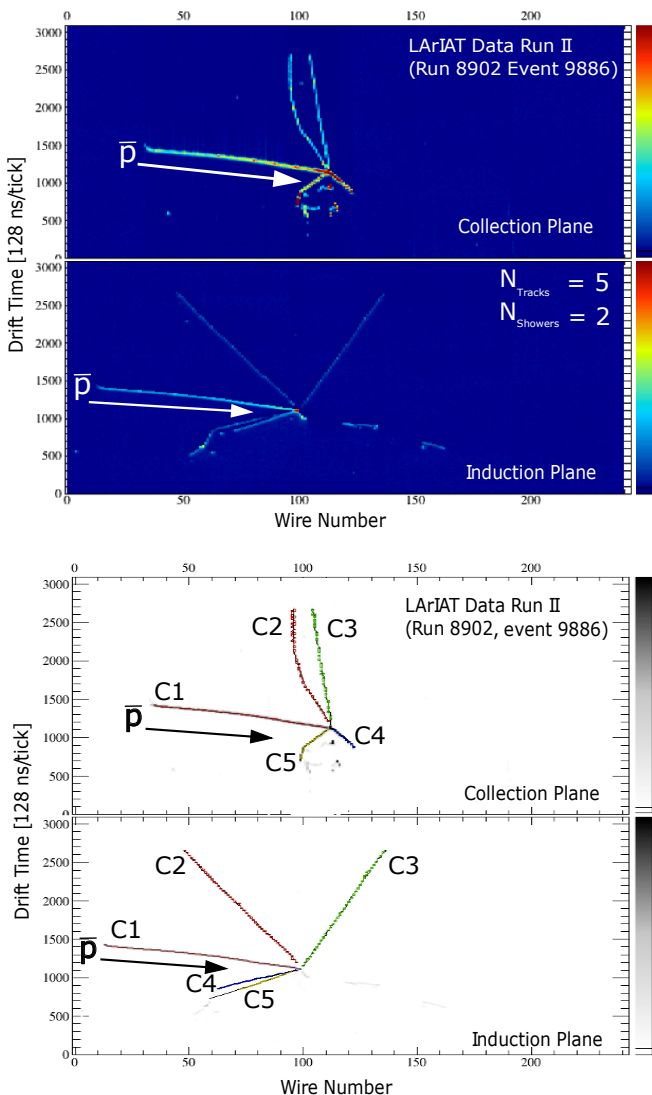


FIG. 6. Typical example of a data antiproton annihilation at rest event (top) and the hand-clustering method applied to the particle track candidates on the same data event (bottom). Hits are manually clustered together for each track candidates individually. Each of the different clustered objects, noted from C1 to C5, are passed to the tracking algorithm to form track objects. In this case, the incoming antiproton is noted by C1 and the outgoing particles noted from C2 to C5.

forms are determined by Gaussian fits to over-threshold pulses found in filtered and deconvolved wire waveforms. Hits are typically clustered together by an automated reconstruction algorithm which reconstructs 3D tracks by time-matching clusters of hits across the two 2D wire-planes [30]. LArIAT’s automated reconstruction algorithms are optimized for forward-going particles and perform poorly on isotropic $\bar{p}N$ candidates by not being able to reconstruct clear and isolated particle tracks from various events. To improve performance, two manual components to the reconstruction are introduced in this analysis.

Hits associated with distinct particles are manually selected by grouping them together into 2D clusters on each wire plane in a customized event display graphical user interface. These clusters are then used to reconstruct 3D tracks using the standard projection-matching track fitting algorithm in LArSoft [31, 32]. Hits located directly at the annihilation vertex are excluded from clusters associated with outgoing particles to avoid complications in the tracking algorithm. This ensures that hits from the stopping antiproton’s Bragg peak or from overlapping outgoing ionization trails are not mistakenly included in the wrong clusters. For candidate incoming antiproton tracks, hand-clustering is treated more inclusively by extending the clustering process as close to the annihilation vertex as possible. An example of the results of individual and manual clustering is shown in Fig. 6 where the different clustered objects are individually grouped in different colors and noted from C1 through C5.

The antiproton is visually identified by looking for tracks which start at the front face of the LArTPC and end within the fiducial volume with a clear increasing dE/dx due to the Bragg peak near the endpoint. The reconstructed position at the most downstream point (highest z) of the antiproton track is assigned as the annihilation vertex and sets its direction. Outgoing tracks are defined such that their orientation is pointing away from the vertex to ensure effective range-based PID.

In order to gauge the performance of the reconstruction methods here, a sample of 1,200 antiprotons entering the LArTPC is simulated. They are generated at the final beamline MPWC approximately 100 cm upstream of the TPC, with a momentum distribution roughly matching data in Fig 2. The MC simulation is performed this way to increase the number of \bar{p} annihilations at rest in the active area of the LArTPC mimicking reality as much as possible. The generated particles decay, interact, and deposit their energy following Geant4 [33] (version 10.3.1) using the QGSP_BERT physics library. To simulate antiproton annihilation on individual nucleons in argon, the Fritiof (FTF) [34, 35] model is used in this paper.

B. LArTPC Particle Identification and Event Selection

Selected beamline events are classified using two hand-scanned selection criteria in the LArTPC:

1. A clear, non-overlapping, incoming beamline particle track must come to a stop with a visible Bragg peak.
2. Outgoing particles must start at the end of the incoming beamline particle and travel away from the annihilation vertex.

The first criterion removes events where the annihilation might have occurred before entering the active region of the LArTPC resulting, in some cases, an empty

event. In data, this criterion additionally removes events containing significant pile-up muon activity which may produce ionization that overlaps and interferes with the actual triggered antiproton track. These pile-ups are caused by additional tracks from muons produced in the upstream beamline elements traveling alongside the true beamline candidates. Since annihilation at rest produces outgoing particles isotropically which are required to be observed from the second criterion, it is possible that tracks in the LArTPC overlap with the incoming stopping antiproton. The clear Bragg peak of the selected events ensures that the particle is coming to rest with its track information passed to the dE/dx -based PID algorithm to identify the particle type.

The particle type associated with a reconstructed track inside the LArTPC is identified by examining the calorimetry information for the track's reconstructed hits. This is done by looking at the amount of energy deposited per unit length (dE/dx) along the 3D track object and comparing it to the expected values of dE/dx for different particle types. In this analysis, particles can be grouped as: proton-like, kaon-like, pion/muon-like, and minimum-ionizing particles without a Bragg peak (non-stopping-like). The PID method consists of calculating a χ^2/NDF between a track's modified residual range profile and expected dE/dx profiles for different particle types, with the number of degrees of freedom (NDF) being the number of reconstructed hits used to calculate the total χ^2 . This algorithm's performance heavily depends on a well-defined and clear Bragg peak. Thus reconstructed hits directly at the annihilation vertex are omitted. This reduces tracking algorithm ambiguity due to charge from the stopping antiproton's Bragg peak or with hits from overlapping outgoing ionization trails. The PID method utilized also accounts for the potentially shorter track length due to under clustering. The values of the residual range are corrected up to the largest expected uncertainty in the reconstructed annihilation vertex position (two wire spacings).

After applying the selection criteria to the 1,200 simulated antiproton events, 80 stopping candidates are selected. By looking at the MC truth information: 69 are true annihilations at rest, while the other 11 retain some kinetic energy at the moment of annihilation. Among these, 9 events have a true final kinetic energy less than 60 MeV and are considered *quasi-rest* candidates. The two remaining events, each with nearly 200 MeV of remaining true kinetic energy, cannot be classified as quasi-rest candidates. Based on the obtained number of misidentified candidates, the *mis-ID* rate of the hand-scan method is estimated to be $< 6\%$. Of the initial 1,200 events, 130 are considered as signals by having true final kinetic energy of less than 60 MeV resulting in a selection efficiency of 60% by considering annihilation at rest and quasi-rest together.

All of the 80 MC signal candidates are also processed through the PID algorithm. The results indicate that 70 of the 80 events are identified as proton-like, 6 as

Selection Cut	Data	Simulation
mass candidates	520	1,200
pile-up or empty events	145	800
stopping candidates	11	80
PID	11	70

TABLE I. Summary of the selection cuts for the antiproton annihilation at rest for both the meabline and LArTPC stages.

kaon-like, and 4 as stopping muon/pion-like. To evaluate the performance of the PID algorithm, the dE/dx distributions for the three categories of antiproton candidates are compared with the expected values, as shown in top of Fig. 7. The proton-like candidates closely align with the proton expectation curve. The kaon-like candidates are positioned between the proton and kaon expectations, leading the PID to favor the kaon hypothesis due to a slight bias towards this behavior. The stopping muon/pion-like events correspond well with the pion/muon expectation curve, thus can not be selected as antiprotons annihilating at rest. The two antiproton candidates that have over 200 MeV of kinetic energy are identified as 1 kaon-like and 1 muon/pion-like. Based on these observations, all 10 non-proton-like candidates are excluded from the sample resulting in a PID algorithm efficiency of 90%.

Following the established selection criteria, the number of data events is reduced from 520 initial candidates in the selected mass range, down to 11 stopping antiprotons annihilation at rest candidate. All 11 candidates are identified as proton-like using the PID χ^2 calculation. For completeness, the dE/dx as a function of the residual range distribution of the antiproton candidates is shown in bottom of Fig. 7 and all align well with the proton-like expected curve. All 11 candidates are expected to be true antiproton annihilations at rest given the relatively small mis-identification rate evaluated from MC. Furthermore, the distribution of the reconstructed beamline mass of these candidates is centered around the antiproton mass peak shown in Fig. 8 with a fitted Gaussian centered at $\sim 933 \text{ MeV}/c^2$ enforcing the case that these are true antiprotons.

A summary of the effect of each selection cut is shown in Table I with the first line corresponding to the beamline selection for data, and all of the MC generated events. The second and third line corresponds to the hand-scanned selection while the fourth and final line to the PID using the LArTPC reconstructed hits. Pile-ups are not simulated in this analysis thus a difference in the relative number of events removed from data and MC is expected for the second selection cut.

A collection of representative selected antiproton annihilation at rest event displays from data and MC simulation is provided in Appendix A.

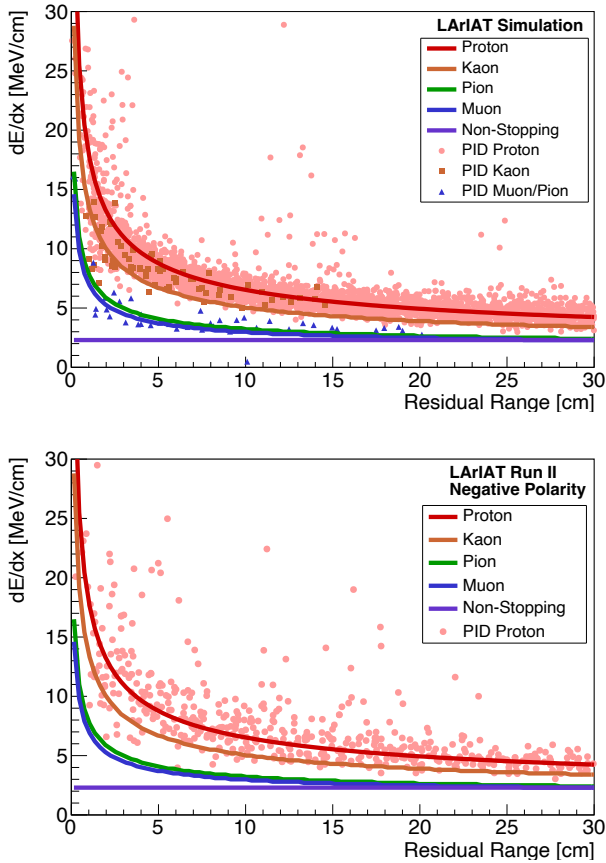


FIG. 7. Distributions of the measured dE/dx for points along candidate tracks as a function of the residual range for all 80 MC candidates passing the selection cuts (top), as well as for all 11 antiproton candidates from data (bottom).

V. FINAL-STATE RECONSTRUCTION RESULTS

As with the incoming antiproton candidates, the particle tracks leaving of the annihilation vertex are passed through the PID algorithm to determine their particle type with the results for the data and simulated events shown in Fig. 9. The simulation was normalized to the number of data antiproton events to allow direct comparisons. Both the data and simulation effectively agree within statistical uncertainty. Half of the outgoing particles have an end point within 1 cm from an edge indicating that they are considered to be exiting the LArTPC. This makes it impossible to perform a definitive PID based on the dE/dx of these tracks and instead contribute to the last bin in Fig. 9.

The final-state outgoing track multiplicity is obtained in two different ways: by hand-counting the number of tracks leaving the annihilation vertex, and by counting the number of reconstructed tracks determined by the automated tracking algorithm. The first method is included due to the reconstruction failures mentioned in

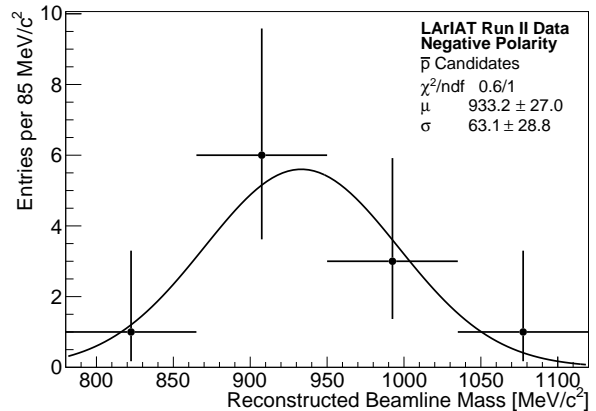


FIG. 8. Distribution of the reconstructed beamline mass of the 11 stopping antiproton candidates with their statistical uncertainty with a fitted Gaussian overlaid resulting in a mass peak of $\sim 933 \text{ MeV}/c^2$.

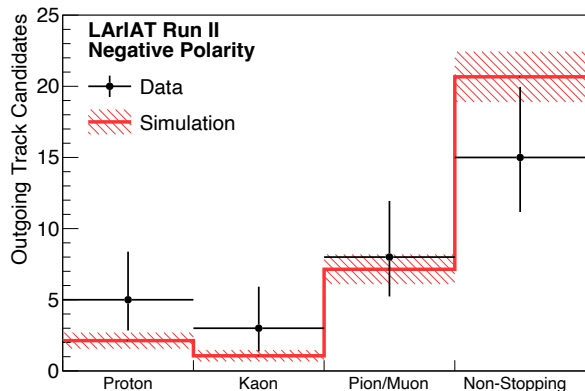


FIG. 9. Distribution of the outgoing particle type from the PID algorithm. The number of signal antiproton tracks from the MC was normalized to the data, and both are shown with their respective statistical uncertainty.

Sec. IV A. This allows for a comparison between the two methods and is possible due to the small size of the final candidate sample in this analysis. Due to complications from manually clustering multiple tracks emanating from a common vertex, hits near the vertex were often excluded, as explained in Sec. IV B. Therefore, a generous maximum track-to-vertex distance of 5 cm was allowed for outgoing track candidates, with a required span of at least several wires to ensure they extend far enough out from the vertex region.

The track multiplicity for the two methods for the simulation and data events is shown in Fig. 10. The calculated track multiplicity agrees well with the simulation within statistical uncertainty.

A summary of the computed means, uncertainty on the means, and the root mean squares (RMS) values for

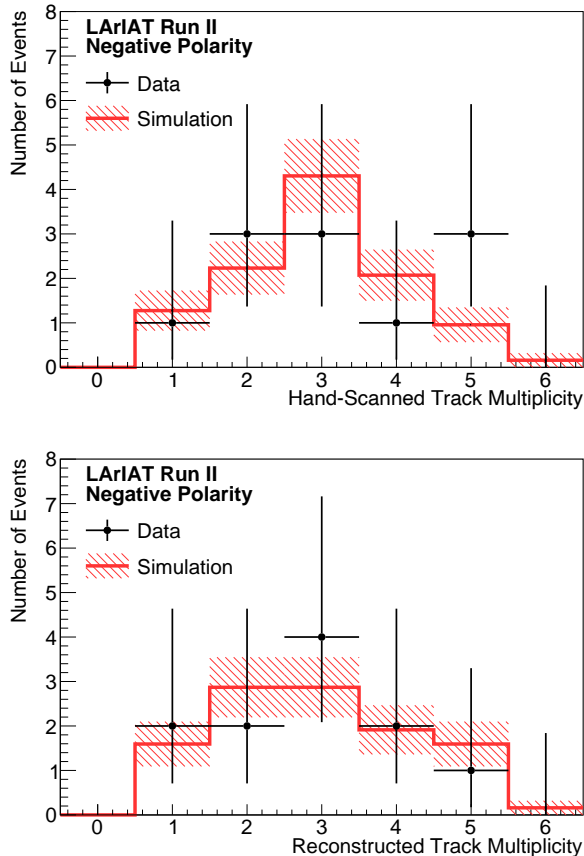


FIG. 10. Distribution of charged particle track multiplicity for outgoing particles from antiproton annihilation at rest: (top) the hand-scanning method, and (bottom) reconstruction algorithm method. Inefficiencies in the reconstruction reduce the overall number of reconstructed tracks. The simulated sample is normalized to the number of events in data.

Method	Data	Simulation
Hand-scanning	3.2 ± 0.4 $\sigma = 1.3$	3.0 ± 0.4 $\sigma = 1.2$
Automated reconstruction	2.8 ± 0.4 $\sigma = 1.2$	2.96 ± 0.16 $\sigma = 1.3$

TABLE II. A summary of the mean with the uncertainty on the mean and RMS (σ) of measured final-state track multiplicity for the antiproton annihilation candidate samples in LArIAT.

both cases is found in Table II where the mean for the reconstructed counting method is slightly lower than for the hand-scanned due to reconstruction failures and inefficiencies.

Antiproton annihilation may also produce π^0 and $\eta^{(\prime)}$ [13, 14], both of which decay into photon showers (γ). They decay promptly which can result in a pair of showers pointing directly back to the annihilation vertex

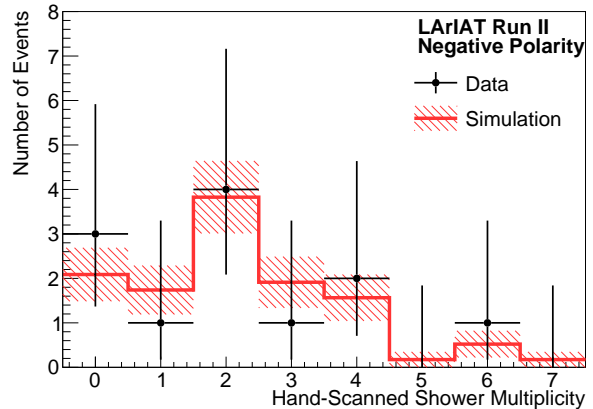


FIG. 11. Distribution of shower multiplicity from antiprotons annihilating at rest using the hand-scanning method. The simulated sample is normalized to the number of events in data.

at some distance. Showers pointing back to the vertex are counted through hand-scanning but the ones pointing back at an outgoing track are not counted as they are considered to originate from one of the outgoing particle tracks rather than directly from the annihilation. Due to the conversion length of γ (greater than 29 cm [36]), and the small size of LArIAT, they can exit the LArTPC before producing a visible shower. The simulation predicts that $>40\%$ of the γ exit the LArTPC before interacting. This results in an observed lower limit on the number of showers coming from the annihilations. Similar to the track multiplicity, the shower multiplicity for data (simulation) corresponds to 2.2 ± 0.5 (2.2 ± 0.5) showers with RMS of 1.8 (1.6) with the distributions shown in Fig. 11. Here as well, the shape of the distributions agree within statistical uncertainty.

VI. CONCLUSIONS

Using a LArTPC detector in a test beam, LArIAT has observed the first antiproton annihilation at rest interactions on argon. Using LArIAT's Run II negative polarity data, a total of 11 candidates of antiproton annihilation at rest are identified using various beamline and LArTPC selections. Within our statistics, data and simulation distribution of the final-state multiplicities and particle type for surface antiproton annihilation at rest using the FTF model as implemented in Geant4 agree well. For data, a mean of 3.2 ± 0.4 tracks per annihilation is measured with RMS of 1.3. Similarly, measurements of shower multiplicity also agree between data and MC, with data showing a mean of 2.2 ± 0.5 showers within LArIAT's active volume with RMS of 1.8. These results strengthen the confidence in the robustness and reliability of current model-building efforts for $n-\bar{n}$ annihilation inside the nucleus by adding a new nucleus to the list

of observed and measured antiproton annihilation at rest events.

VII. ACKNOWLEDGEMENTS

This document was prepared by the LArIAT collaboration using the resources of the Fermi National Accelerator Laboratory (Fermilab), a U.S. Department of Energy, Office of Science, HEP User Facility. Fermilab is managed by Fermi Research Alliance, LLC (FRA), acting under Contract No. DE-AC02-07CH11359. We also gratefully acknowledge the support of the National Science Foundation; Brazil CNPq grant number 233511/2014-8, Coordenação de Aperfeiçoamento de Pes-

soal de Nível Superior - Brazil (CAPES) - Finance Code 001, São Paulo Research Foundation - FAPESP (BR) grant number 16/22738-0; Polish National Science Centre grant Dec-2013/09/N/ST2/02793; the Science and Technology Facilities Council (STFC), part of the United Kingdom Research and Innovation; The Royal Society (United Kingdom); Marie Skłodowska-Curie grant agreements numbers 822185 and 892933; STFC grant number ST/W003945/1; and the JSPS grant-in-aid (Grant Number 25105008), Japan. The collaboration extends a special thank you to the coordinators and technicians of the Fermilab Test Beam Facility, without whom none of this work would have been possible. The authors want to also thank Dr. Adam Lister for insightful discussion throughout the review of this paper.

-
- [1] O. Chamberlain, E. Segrè, C. Wiegand, and T. Ypsilantis, *Phys. Rev.* **100**, 947 (1955).
- [2] O. Chamberlain *et al.*, *Il Nuovo Cimento* **3**, 447 (1956).
- [3] W. H. Barkas *et al.*, *Phys. Rev.* **105**, 1037 (1957).
- [4] J. Díaz *et al.*, *Nucl. Phys. B* **16**, 239 (1970).
- [5] N. Barash, P. Franzini, L. Kirsch, D. Miller, J. Steinberger, T. H. Tan, R. Plano, and P. Yaeger, *Phys. Rev.* **139**, B1659 (1965).
- [6] C. Baltay, P. Franzini, N. Gelfand, G. Lütjens, J. C. Severiens, J. Steinberger, D. Tycko, and D. Zanello, *Phys. Rev.* **140**, B1039 (1965).
- [7] C. Baltay, P. Franzini, G. Lütjens, J. C. Severiens, J. Steinberger, D. Tycko, and D. Zanello, *Phys. Rev.* **140**, B1042 (1965).
- [8] M. Chiba *et al.*, *Phys. Rev. D* **36**, 3321 (1987).
- [9] M. Chiba *et al.*, *Phys. Rev. D* **39**, 3227 (1989).
- [10] S. Ahmad *et al.*, *Phys. Lett. B* **152**, 135 (1985).
- [11] E. Aker *et al.* (Crystal Barrel), *Nucl. Instrum. Meth. A* **321**, 69 (1992).
- [12] M. Agnello *et al.*, *Nucl. Instrum. Meth. A* **399**, 11 (1997).
- [13] C. Amsler, *Rev. Mod. Phys.* **70**, 1293 (1998), arXiv:hep-ex/9708025.
- [14] C. Amsler *et al.* (Crystal Barrel), *Nucl. Phys. A* **720**, 357 (2003).
- [15] S. Aghion *et al.*, *JINST* **9**, P06020 (2014).
- [16] S. Aghion *et al.*, *JINST* **12**, P04021 (2017).
- [17] T. Von Egidy, *Nature* **328**, 773 (1987).
- [18] R. N. Mohapatra, *J. Phys. G* **36**, 104006 (2009), arXiv:0902.0834 [hep-ph].
- [19] A. D. Sakharov, *Sov. Phys. Usp.* **34**, 392 (1991).
- [20] M. Fukugita and T. Yanagida, *Phys. Lett. B* **174**, 45 (1986).
- [21] K. S. Babu, R. N. Mohapatra, and S. Nasri, *Phys. Rev. Lett.* **97**, 131301 (2006).
- [22] K. S. Babu, P. S. Bhupal Dev, E. C. F. S. Fortes, and R. N. Mohapatra, *Phys. Rev. D* **87**, 115019 (2013).
- [23] S. Nussinov and R. Shrock, *Phys. Rev. Lett.* **88**, 171601 (2002).
- [24] E. Klempt, C. Batty, and J.-M. Richard, *Phys. Rept.* **413**, 197 (2005), arXiv:hep-ex/0501020.
- [25] M. Astrua *et al.*, *Nucl. Phys. A* **697**, 209 (2002).
- [26] R. Acciarri *et al.* (LArIAT), *JINST* **15**, P04026 (2020), arXiv:1911.10379 [physics.ins-det].
- [27] “FTBF (fermilab test beam facility),” <http://ftbf.fnal.gov>.
- [28] E. Gramellini *et al.* (LArIAT Collaboration), *Phys. Rev. D* **106**, 052009 (2022), arXiv:2108.00040 [hep-ex].
- [29] E. Snider and G. Petrillo, *J. Phys. Conf. Ser.* **898**, 042057 (2017).
- [30] B. Baller, *JINST* **12**, P07010 (2017).
- [31] T.-J. Yang (DUNE), *PoS ICHEP2016*, 183 (2016).
- [32] M. Antonello *et al.*, *Adv. High Energy Phys.* **2013**, 260820 (2013), arXiv:1210.5089 [physics.ins-det].
- [33] S. Agostinelli *et al.*, *Nucl. Instrum. Meth. A* **506**, 250 (2003).
- [34] B. Andersson, G. Gustafson, and B. Nilsson-Almqvist, *Nucl. Phys. B* **281**, 289 (1987).
- [35] B. Nilsson-Almqvist and E. Stenlund, *Comput. Phys. Commun.* **43**, 387 (1987).
- [36] C. Adams *et al.* (MicroBooNE), *JINST* **15**, P02007 (2020), arXiv:1910.02166 [hep-ex].

Appendix A: Selected Data Antiproton Candidates

Figure 12 show a selection of representative data and MC event displays for antiproton annihilation at rest. The highly ionizing track traveling from the middle-left towards the center of the panels are the incoming antiproton marked in white with \bar{p} and arrow for the direction. At the end of the antiproton’s Bragg peak, outgoing tracks are seen exiting directly from the annihilation vertex, while outgoing showers exhibit a gap between the vertex and their starting point but are still oriented directly towards the vertex. The number of hand-scanned tracks (N_{tracks}) and showers (N_{showers}) for these events are indicated in the event displays. In the case of (a) and (c), the relatively straight tracks near the top half of the collection and induction plane panes are high-energy ‘halo’ muons produced from the pion decays in the secondary beam far upstream of the LArIAT tertiary beamline, which can contaminate beamline-triggered readouts with multiple extra tracks unassociated with the tertiary beamline.

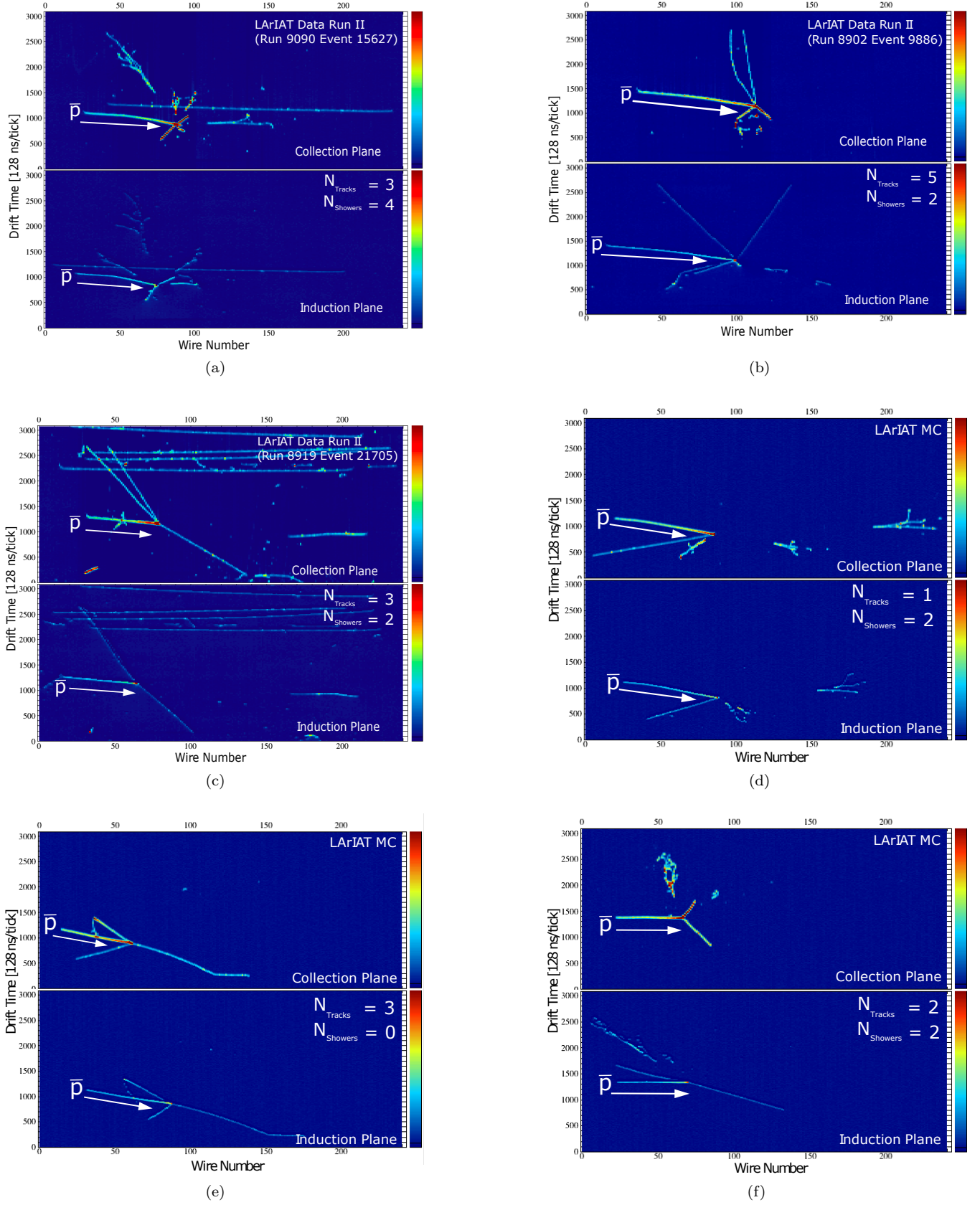


FIG. 12. Antiproton annihilation data (a)-(c) candidates and MC (d)-(f) obtained from the selection. The incoming identified antiprotons are marked with \bar{p} and their direction with the arrows both in white.